

GRUP DE DISPOSITIUS
FOTOVOLTAICS I OPTOELECTRÒNICS

DEPARTAMENT DE FÍSICA

Universitat Jaume I
CASTELLÓ - SPAIN
<http://www.elp.uji.es>



MASTER'S IN APPLIED PHYSICS

Thesis

A Photoelectrochemical study of Bismuth Vanadate
Photoanodes for Solar Water Splitting

Sandheep Ravishankar

Submitted to

Dr. Sixto Giminez

August 2015

Acknowledgements

I would primarily like to thank my thesis supervisor, Dr. Sixto Gimenez for his guidance and help during the course of this investigation. I would also like to thank Dr. Francisco Fabregat Santiago and Prof. Juan Bisquert for providing several useful inputs and clarifications regarding solar water splitting and impedance spectroscopy.

The lively discussions with Dr. Isaac Herraiz – Cardona, Dr. Rafael Sanchez and Luca Bertoluzzi regarding all aspects of solar water splitting are gratefully acknowledged.

I sincerely thank Dr. Wilson Smith and Bartek Trzesniewski for the measurements made at TU-DELFT and their guidance and hospitality during my research visit.

Last but not the least, I would like to acknowledge Generalitat Valenciana for funding under the Project GRISOLIA/2014/034.

Abstract

Bismuth Vanadate (BiVO_4) is a promising photoanode in the field of solar water splitting due to its low cost of synthesis, low toxicity, good stability and high theoretical photocurrent density. However, several reports on this material have shown poor photocurrent densities, poor photon conversion efficiencies, high surface recombination and slow kinetics at the BiVO_4 /electrolyte interface.

In order to identify and address these issues, a review of the properties of this material and the research carried out on it is provided, followed by a thickness dependent study to make an overall characterisation of the material in terms of morphology, phase and photoelectrochemical performance.

We also confirm the high surface recombination and slow kinetics at the $\text{BiVO}_4/\text{H}_2\text{O}$ interface, while shedding light on the reported mechanisms of slow electron transport and photocurrent enhancement by an interfacial SnO_2 layer (hole mirror effect).

Electrochemical impedance spectroscopy measurements determine a capacitance with magnitudes similar to a depletion-region capacitance with a capacitive peak at ~ 0.75 V vs V_{RHE} , related to the $\text{V}^{4+}/\text{V}^{5+}$ redox couple, which made the estimation of the actual flatband potential difficult.

Contents

Index of Figures	7
Index of Tables.....	9
Section 1 Introduction and Objectives.....	10
Section 2 Literature Review	14
2.1 Crystal and Electronic Structure	14
2.2 Synthesis	15
2.3 Strategies to improve PEC performance.....	15
2.3.1 Composite Electrodes	15
2.3.2 Porous and Nanostructured Morphologies	17
2.3.3 Facet Dependence	18
2.3.4 Doping Studies	18
2.3.5 Oxygen Evolution Catalysts	19
Section 3 Experimental Techniques and Parameters.....	20
3.1 Spincoating	20
3.2 X-Ray Diffraction	21
3.3 UV-Visible Spectrophotometry	21
3.4 Cyclic Voltammetry	22
4.5 Electrochemical Impedance Spectroscopy	23
Section 4 Results and Discussion	24
4.1 Microscopy	24
4.2 X-ray diffraction.....	25
4.3 Optical measurements	26
4.4 PEC tests	27

4.5 Interfacial Tin Oxide layer	29
4.6 EIS measurements	30
Section 5 Conclusion and future work	34
Bibliography	35

Index of figures

Figure 1 Energy diagrams for a) n-type single bandgap photoanode b) n-type photoanode and p-type photocathode connected in series c) n-type photoanode connected to a PV cell for additional bias d) dual bandgap cell with PV cells connected to both photoanode and photocathode	11
Figure 2 Band edges of Valence and conduction bands of different PEC electrodes	12
Figure 3 Band energetics for n-type photoanode in the case of a) dark conditions, before contact b) Equilibration of fermi level with redox potential in the electrolyte, formation of space charge region of width w c) Change in hole quasi-fermi level upon illumination, providing suitable overpotential for transfer of minority carriers to solution	12
Figure 4 Position of bands and fermi level under a) dark conditions b) illumination	13
Figure 5 Crystal structures of a) Tetragonal Scheelite b) Zircon type BiVO_4 (Red – V, Purple – Bi and Gray – O) Local coordination of V and Bi ions in c) Monoclinic Scheelite d) Tetragonal Scheelite and e) Zircon type BiVO_4 with all bond lengths in Å	14
Figure 6 Proposed models - a,b) Trapping of electrons at a defect state at the FTO/ BiVO_4 interface followed by recombination with holes in the valence band c) ‘Hole mirror’ effect of SnO_2	16
Figure 7 Cascade driving potential for electrons photogenerated in BiVO_4 towards the back contact with photogenerated holes reflected at the $\text{SnO}_2/\text{BiVO}_4$ interface	17
Figure 8 Proposed model for slow electron transport in BiVO_4 – In the case of back illumination, electrons are photogenerated closer to the back contact while under front illumination, photogenerated electrons are required to diffuse over the entire length of the semiconductor before extraction	19
Figure 9 Mechanism of hole extraction at the semiconductor surface by Co-Pi	20
Figure 10 Principle of X-ray diffraction from adjacent planes of a crystal lattice	21
Figure 11 Schematic view of the UV-VIS absorption setup	22
Figure 12 Three electrode setup with working (WE), counter (CE) and reference (RE) electrodes.....	23
Figure 13 Small signal linear response of the perturbing voltage required for EIS	23
Figure 14 Basic electric components used for modelling EIS data and their corresponding impedances.....	24

Figure 15 SEM image of SnO ₂ /BiVO ₄ sample.....	25
Figure 16 XRD spectrum for samples with their respective number of spincoating cycles.....	25
Figure 17 Absorbance of BiVO ₄ samples prepared by 3, 5, 7, 9, 11 and 13 cycles of spin-coating	26
Figure 18 Comparison of substrate (back) illumination of BiVO ₄ samples prepared by 3, 5, 7, 9, 11 and 13 cycles of spin-coating.	27
Figure 19 Variation of current density versus thickness of BiVO ₄ represented by the number of spincoating cycles	28
Figure 20 J-V curves in the dark, under illumination and in the presence of a hole scavenger under illumination	29
Figure 21 Comparison in performance of BiVO ₄ (7 cycles spincoating) with and without an interfacial Tin Oxide layer	29
Figure 22 a)Nyquist plot of 7 cycles spincoating BiVO ₄ sample at 1.4 V vs V _{Ag/AgCl} b) Fitting circuit used for the EIS data in dark.....	30
Figure 23 Variation of capacitance with applied voltage and of BiVO ₄ samples of different thicknesses obtained from EIS measurements in dark conditions.....	31
Figure 24 Mott-Schottky plots of BiVO ₄ samples of different thicknesses obtained from EIS measurements in dark conditions	32

Index of Tables

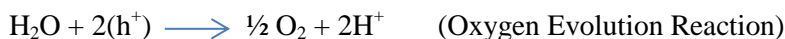
Table 1 Calculated thickness (absorption coefficient = $3 \times 10^4 \text{ cm}^{-1}$ at 400 nm) of BiVO_4 samples prepared by 3, 5, 7, 9, 11 and 13 cycles of spincoating.....	26
Table 2 Obtained flatband potentials, doping density values from EIS measurements and flatband potentials obtained from literature.....	32

Harvesting the energy of the sun possesses great potential to solve the current global energy crisis. The energy from the sun is a clean, renewable and inexhaustible resource with the magnitude of power striking the Surface of the earth at any instant equal to that produced by 130 million 500 MW power plants [1].

Several factors like material for energy conversion and storage must be taken into account. Since the energy flux from the sun is seasonal, provisions must be made to store this energy in chemical form for easy transport and usage on demand. These needs must also be met in a cost-efficient and environmentally friendly way.

In this regard, solar water-splitting is a viable solution, which involves utilising semiconductor materials to photo-catalyse the reduction and oxidation of water ie: store the energy of the sun in the chemical bonds of H₂. These reactions are environmentally clean and produce hydrogen gas and oxygen gas, with hydrogen touted to be an important fuel that will power the economies of the future.

For all its promise, water splitting is an uphill reaction to carry out thermodynamically. The free energy change for the conversion of one molecule of H₂O into H₂ and ½ O₂ is 237.2 kJ/mol which corresponds to 1.23 V according to the Nernst equation. This essentially means that the semiconductor carrying out water splitting must possess a bandgap in excess of 1.23 V for these reactions (shown below) to be thermodynamically feasible [2].



The reduction potential of H₂ is known as the Standard Hydrogen Electrode (SHE) and is used as reference for all other potentials. It is taken to be 0 V. This means that the water oxidation potential occurs at +1.23 V vs V_{SHE}.

A basic solar water splitting cell consists of a photoanode and a photocathode in contact with the electrolyte. Upon irradiation, electron-hole pairs are generated in the semiconductor. In the case of a photocathode, electrons photo-generated in the conduction band, drive the reduction of H₂O into H₂ while holes transferred from the photoanode to the electrolyte oxidise the water at the photoanode/electrolyte interface.

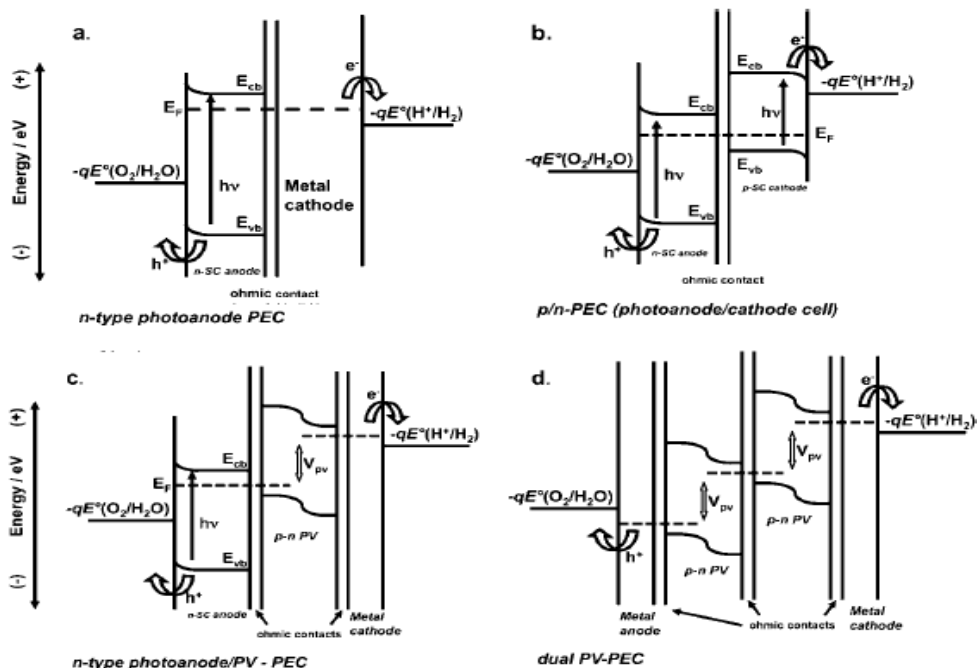


Figure 1 Energy diagrams for a) n-type single bandgap photoanode b) n-type photoanode and p-type photocathode connected in series c) n-type photoanode connected to a PV cell for additional bias d) dual bandgap cell with PV cells connected to both photoanode and photocathode [2]

Solar water splitting cells are divided into two categories. A single bandgap device is termed **S2** and has a maximum conversion efficiency of 30% under 1 sun illumination (100 mW/cm^2) and requires a minimum of two photons to generate a single molecule of H_2 , whereas a dual bandgap device is termed as **D2** or **D4**, requiring two or four photons to produce one molecule of H_2 . A dual bandgap device requires stacking of two different materials, with different bandgaps in order to absorb a greater region of energy from the solar spectrum. The theoretical maximum efficiency of a **D2** device is 41% [1,2].

Another important consideration is the position of the valence and conduction bands with respect to the redox potentials and the overpotentials required to drive these reactions. A material whose valence band potential is not sufficiently positive or conduction band whose potential is not sufficiently negative will not be able to carry out water oxidation or reduction respectively. Since it is very difficult to find a material that straddles both the water oxidation and hydrogen reduction potentials, in general, different semiconductors are used as photoanode and photocathode. Figure 2 shows a list of several semiconductors and the positions of their valence and conduction bands with respect to water oxidation potential.

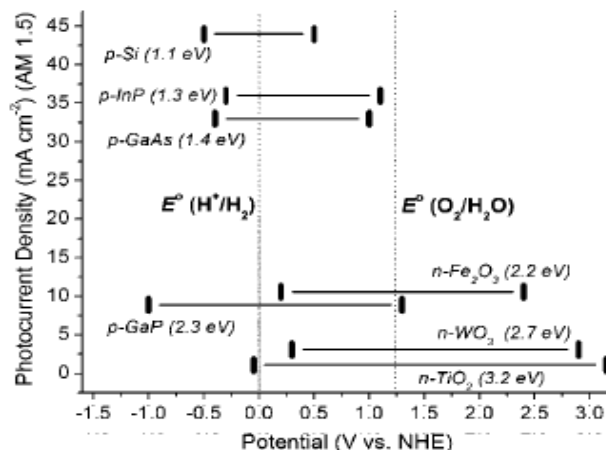


Figure 2 Band edges of Valence and conduction bands of different PEC electrodes [2]

In general, n-type electrodes are used as photoanodes and p-type electrodes as photocathodes.

The reasoning behind this is the fact that a driving potential in the form of band bending occurs at the interface in the dark, which drives minority carriers to the solution when the electrode is illuminated (figure 3).

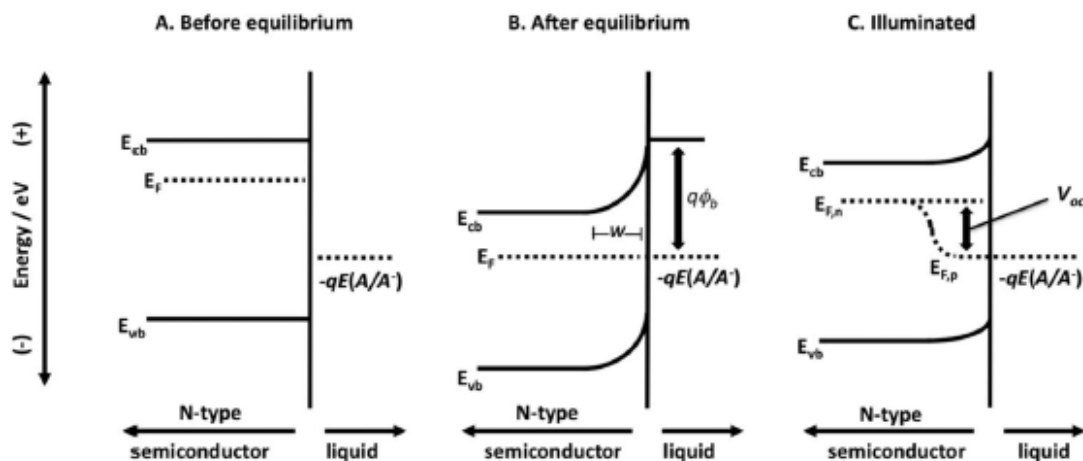


Figure 3 Band energetics for n-type photoanode in the case of a) dark conditions, before contact b) Equilibration of fermi level with redox potential in the electrolyte, formation of space charge region of width w c) Change in hole quasi-fermi level upon illumination, providing suitable overpotential for transfer of minority carriers to solution [2]

The interest in using BiVO_4 as a photoanode stems from its good stability, low cost, reliable theoretical photocurrent (upwards of 7 mA/cm^2), absorption in the visible and the very positive position of its valence band, $\sim 2.4 \text{ V vs } V_{\text{RHE}}$ with the conduction band slightly more positive than $V_{\text{RHE}} (+ 0.02 \text{ V vs } V_{\text{RHE}})$ (figure 4)[3]. This large difference in potential, coupled with the

inherent n-type nature generates a large driving field for the transfer of minority carriers ie: holes to solution to carry out the water oxidation.

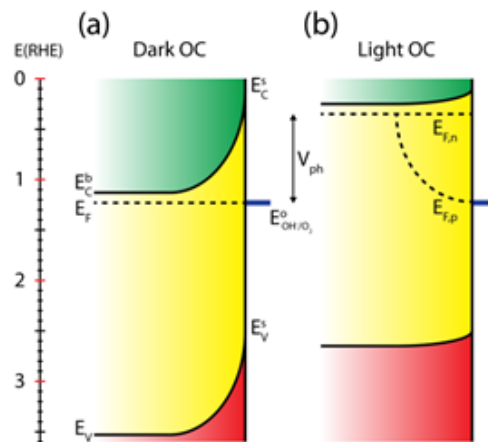


Figure 4 Position of bands and fermi level under a) dark conditions b) illumination [12]

While BiVO_4 possesses many advantages for use as a photoanode, the performance of this material has been quite poor, with an onset potential shifted several hundreds of mV from its reported flatband potential. Several limiting factors like high amount of recombination of electron-hole pairs, slow electron transport and slow water oxidation kinetics at the interface have been reported[4-6]. (The latter is widely known as is the case for multi-electron or hole transfer reactions)

The objectives of this report are:

- Determination of optimum PEC performance
- Identification of performance limiting factors like surface/bulk recombination, slow kinetics etc
- Implementation of strategies to improve the PEC performance
- Identification and modelling of bulk and interfacial processes involved in BiVO_4 photoanodes using Electrochemical impedance spectroscopy

2.1 CRYSTAL AND ELECTRONIC STRUCTURE

Bismuth Vanadate prepared in the laboratory exists in two crystal structures, the scheelite or a Zircon-type structure. The Scheelite structure can either exist in a monoclinic (space group $I2/b$ with $a = 5.1935 \text{ \AA}$, $b = 5.0898 \text{ \AA}$ and $c = 11.6972 \text{ \AA}$, $\beta = 90.387^\circ$) phase or a tetragonal (space group $I4_1/a$ with $a = b = 5.1470 \text{ \AA}$, $c = 11.7216 \text{ \AA}$)[7] phase while the Zircon-type exists in a Tetragonal system (space group $I4_1/a$ with $a = b = 7.303 \text{ \AA}$, $c = 6.584 \text{ \AA}$)[8].

In the Scheelite structure, each V ion is coordinated by 4 O atoms to form a tetrahedral structure with each Bi atom coordinated by 8 O atoms from 8 different VO_4 tetrahedral units (figure 10)[7].

The structures of the monoclinic and tetragonal structures are similar except for the distortion in the environment of the V and Bi ions, removing the four-fold symmetry of the tetragonal system[7].

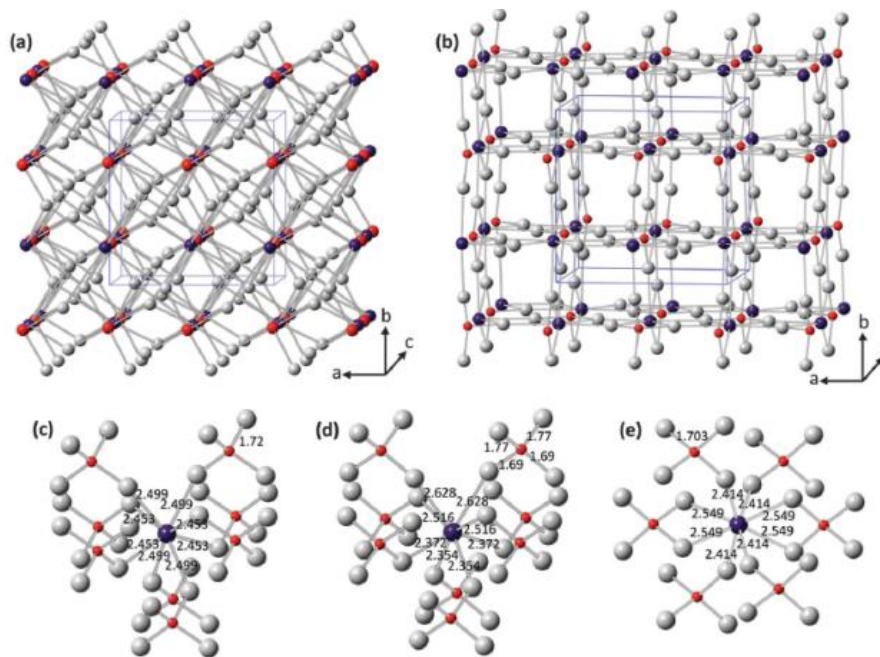


Figure 5 Crystal structures of a) Tetragonal Scheelite b) Zircon type BiVO_4 (Red – V, Purple – Bi and Gray – O) Local coordination of V and Bi ions in c) Monoclinic Scheelite d) Tetragonal Scheelite and e) Zircon type BiVO_4 with all bond lengths in \AA [9]

For solar water splitting purposes, it is of interest to crystallise the Monoclinic scheelite structure due to its absorption in the visible with a bandgap of ~2.4 eV (figure 4) as opposed to the Tetragonal scheelite, which absorbs in the UV region of the spectrum (bandgap ~2.9 eV)[10].

2.2 SYNTHESIS

Several synthesis methods of BiVO_4 have been reported in literature, the most prominent methods of which are mentioned in this section. An efficient method has been Metallorganic deposition (MOD) using spray pyrolysis, as reported in [11, 12]. Electrodeposition is also a reliable method, with both a single step and two step method reported. In the single step method, adopted by Seabold et al [13], the precursor solution, maintained at a slightly acidic pH is used for electrodeposition of BiVO_4 , followed by annealing at 500° C for 1 hour. In the two step process [14], the first step involves cathodic deposition of Bi from an acidic BiCl_3 medium, followed by anodic stripping in an aqueous medium containing V precursor, which then yields crystallised BiVO_4 . Another commonly used method is MOD by spincoating of the precursor [15, 16]. The annealing step in these processes is most important because the crystallization of the monoclinic Scheelite phase occurs at elevated temperatures above 450° C [17].

2.3 STRATEGIES TO IMPROVE PEC PERFORMANCE

2.3.1 Composite electrodes

Liang et al [11] significantly enhanced the performance of BiVO_4 by the addition of an interfacial layer of SnO_2 . The addition of this layer improved the collection efficiency by 20% between 350 and 450 nm. According to the authors, the SnO_2 layer behaves as a 'hole mirror' by passivation of a surface trap in the FTO, which acts as a recombination center (Figure 11).

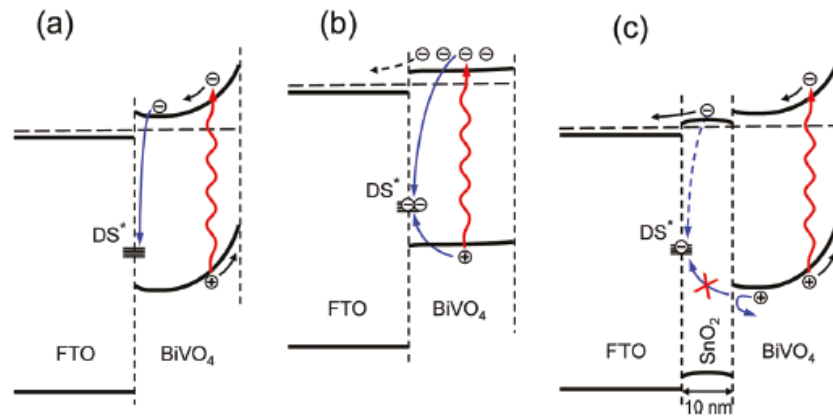


Figure 6 Proposed models - a,b) Trapping of electrons at a defect state at the FTO/BiVO₄ interface followed by recombination with holes in the valence band c) 'Hole mirror' effect of SnO₂ [11]

In the same investigation, it was observed that illumination from the substrate side (back) produced a higher collection efficiency than illumination from the electrolyte side (front) (figure 8). The authors concluded that this occurs due to the slow transport of electrons in BiVO₄. In the case of back illumination, the electrons are extracted easily because they are generated close to the contact but during front illumination, since the electron-hole pairs are generated within the penetration length, they are required to diffuse over the entire length of the semiconductor before extraction. The observed poorer performance during front illumination points to the fact that the greater length over which the electrons are required to diffuse limits the performance, concluding that the electron transport is slow. This argument is supported by observing the electronic and crystal structure. Electronic structure calculations show that the conduction band of BiVO₄ consists of mainly V 3d orbitals [18, 19]. However, the crystal structure shows that the VO₄ tetrahedra are not interconnected with each other, which could be an explanation for the poor transport properties [16].

Several reports have been made regarding WO₃/BiVO₄ electrodes, due to the favourable conduction band edge (+0.42 V vs V_{RHE}) and good stability of WO₃ [3, 16, 20, 21]. Saito et al [21] demonstrated improved PEC performance with a multi- composite WO₃/SnO₂/BiVO₄ electrode. Apart from the increased absorption in the visible region of the spectrum due to WO₃, a cascade driving potential is developed for the electrons due to the favourable positions of the bands of the different semiconductor materials. This leads to efficient extraction of electrons to the contact while the SnO₂ layer prevents holes generated in the BiVO₄ from reaching the WO₃ layer, which reduces recombination at the WO₃/SnO₂ and WO₃/FTO interface.

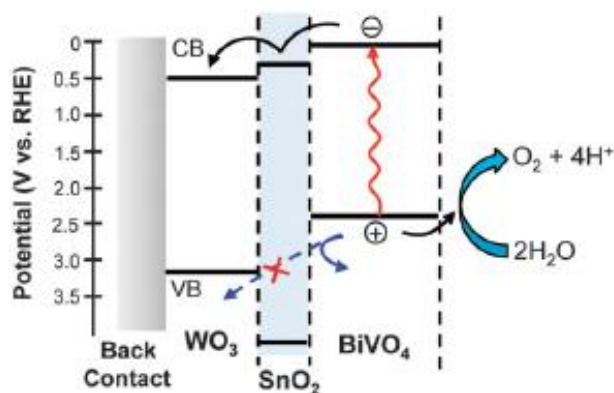


Figure 7 Cascade driving potential for electrons photogenerated in BiVO_4 towards the back contact with photogenerated holes reflected at the $\text{SnO}_2/\text{BiVO}_4$ interface [21]

2.3.2 Porous and nanostructured morphologies

The main advantage of a porous electrode is the large surface area available per unit volume. This allows for improved carrier extraction to the solution as the minority carriers need not diffuse over the entire length of the semiconductor for extraction. A higher porosity can also be detrimental to the performance due to poor transport properties due to formation of surface states, grain sites and poor crystallinity [22].

Luo et al [23] produced porous BiVO_4 electrodes which consisted of worm-like particles with sizes between 50-200 nm. This greatly enhanced the PEC performance, especially in the high-bias (0.9 V vs V_{RHE}) region.

Kim et al [24] developed nanoporous BiVO_4 using a modified electrodeposition method involving initial deposition of a BiOI electrode. The advantage of BiOI is that its 2-D structure enables deposition of very thin films with voids between them. These voids prevent nucleation which results in the formation of nanoporous electrodes. The performance of these electrodes was very high, with a reported photocurrent density of 3.3 mA/cm^2 (0.5 M phosphate buffer with 1 M Na_2SO_3 as hole scavenger) at 0.6 V vs V_{RHE} .

Nanorods and nanowires are other methods to increase the surface area, while improving the transport properties of the carriers. Su et al [25] developed WO_3 nanorods and also pyramidal shaped BiVO_4 nanowire arrays on FTO substrates to improve the PEC performance.

2.3.3 Facet dependence

It is well known that the crystal plane that is exposed at the surface greatly affects the PEC performance [26, 27], including both thermodynamic and kinetic factors [28, 29]. While some studies have been reported [30-32], the most interesting study is by Xi et al [33], who synthesized monoclinic scheelite BiVO_4 nanoplates with well defined {001} facets exposed using a hydrothermal method. The photocatalytic activity was found to be higher than nanorod samples grown along the [001] direction (facet at the surface undetermined) whose surface area was three times greater. The authors were unable to prove that the enhancement in performance is solely due to the exposed {001} planes but the study provides an important aspect of the PEC electrode that must be taken into account while designing the electrodes.

2.3.4 Doping studies

Among several doping studies performed on BiVO_4 , a significant one was carried out by Park et al [34], who discovered that incorporation of 2 atomic percent Mo and 6 atomic percent W in BiVO_4 showed much higher performance compared to undoped samples or any other combination of concentration of dopants. DFT calculations, which assumed the substitution of V by Mo and W, confirmed that Mo and W act as shallow donors which increase the carrier density. An unexpected result was the change in phase from the less symmetric monoclinic scheelite to tetragonal, confirmed by XRD. These results were reproduced by Berglund et al [6]. In both cases, it was observed that the carrier density doubled after doping but the flatband potential remained the same. The increase in performance was attributed to the improved conductivity due to the increased carrier density.

Another interesting effect of the doping was determined from DFT calculations by Zhao et al [35], who concluded that the effective mass of holes decreases slightly upon doping with Mo or W but the effective mass of electrons increases. This finding supports the reasoning of slow electron transport in BiVO_4 . However, DFT calculations performed by Park et al [34] predicted no change in the effective masses of holes and electrons. Their calculations also showed that the excess electrons from W or Mo localize on a V atom to form V^{4+} centers and cause local distortions in the structure. If the transport is governed by polaron hopping (V^{4+} center migration), then the addition of dopants increases the number of V^{4+} centers, increasing overlap

between them and reducing the activation energy for hopping, which improves the PEC performance.

Further doping studies were performed by Zhong et al [4]. The BiVO_4 samples were doped using W as an n-type dopant to increase the concentration of the electrons. Liang et al [11] observed that W doping improved the collection efficiency by $\sim 20\%$ along the entire absorption spectrum, with a maximum of 52% at 370 nm. In both the reports, the difference in performance between back and front illumination was also reduced, which points towards the existence of slow electron transport in BiVO_4 (figure 8).

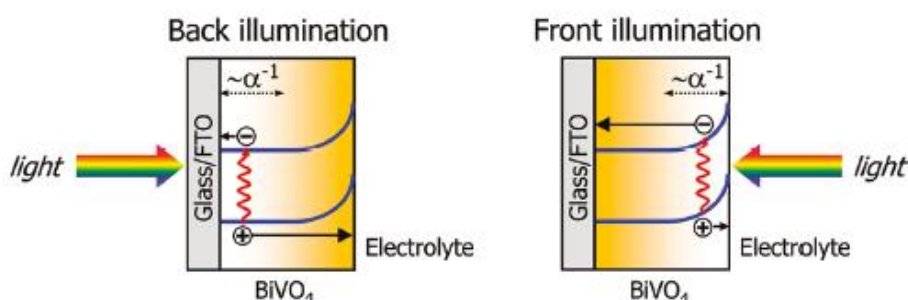


Figure 8 Proposed model for slow electron transport in BiVO_4 – In the case of back illumination, electrons are photogenerated closer to the back contact while under front illumination, photogenerated electrons are required to diffuse over the entire length of the semiconductor before extraction [11]

2.3.5 Oxygen evolution catalysts (OEC)

An oxygen evolution catalyst is used in order to improve the slow water oxidation kinetics at the BiVO_4 /electrolyte interface. The role of the OEC is to enhance the evolution of oxygen by reducing surface recombination by rapid extraction of the holes at the surface.

The most common OEC in the case of BiVO_4 is Co-Pi. Several studies report a cathodic shift in onset potential, enhanced photocurrents and increased stability of the electrode [4, 5, 36-38]. In a study by Zhong et al [4], a W/BiVO_4 – Co-Pi system (figure 9) yielded a collection efficiency of $\sim 20\%$ at 420 nm, 0.6 V vs V_{RHE} , as compared to a W/BiVO_4 electrode that yielded no photocurrent for the same applied potential.

Seabold et al [13] reported the use of FeOOH as an OEC for BiVO_4 . The FeOOH was deposited on the surface of BiVO_4 by using photogenerated holes to oxidise Fe^{2+} to Fe^{3+} , thereby creating a thin film of FeOOH . The electrode showed a remarkable photocurrent for sulfite oxidation, reaching 1 mA/cm^2 at a bias of 0.58 V vs V_{RHE} under AM 1.5 G, 100 mW/cm^2 illumination.

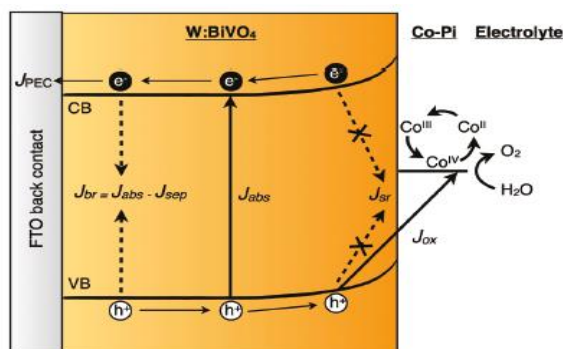


Figure 9 Mechanism of hole extraction at the semiconductor surface by Co-Pi [4]

3

Experimental Techniques and Parameters

3.1 SPINCOATING

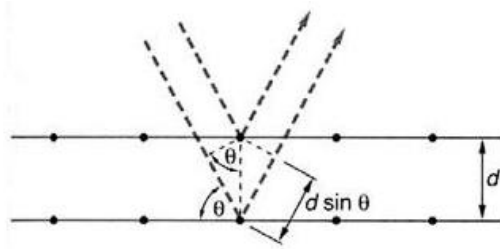
This method involves placing a small volume of the liquid precursor at the center of a substrate and then spinning the substrate at high speed. Centripetal force causes the precursor to spread out over the entire substrate, while air flowing over the substrate causes the evaporation of the precursor, leaving behind a thin layer. Final film thickness depends on several factors like nature of the precursor (viscosity, drying rate, solid content, surface tension etc), spin rate and acceleration.

BiVO₄ samples were prepared by spincoating 50 μ L of precursor - Bi(NO₃)₃·5H₂O (0.1940 g, 0.4 mM) and Vo(acac) (0.106 g, 0.4 mM) in 11.5 ml Acetylacetone on FTO coated glass substrates (Pilkington TEC8, 8 Ω cm²) at 1000 rpm for 30 seconds. The thickness of the samples was varied by the number of spin-coating cycles: 3, 5, 7, 9, 11 and 13 cycles. (In this report, for convenience, the samples are referred to with their respective number of cycles of spincoating) After each spin-coating cycle, the samples were annealed at between 450 - 550° C for 15 minutes with a final annealing step for 2 hours at 500° C.

3.2 X-RAY DIFFRACTION

A technique that provides information regarding the composition, phase and planes of the constituent atoms, in which the atoms diffract a beam of incident x-rays, which then interfere on a screen at specific angles, according to Bragg's law. The condition for constructive interference is given by

$$n\lambda = 2d\sin\theta$$



λ – incident beam wavelength

d – lattice plane spacing

θ – angle of incidence

n – order of diffraction

Figure 10 Principle of X-ray diffraction from adjacent planes of a crystal lattice

3.3 UV – VIS SPECTROPHOTOMETRY

This technique is based on the Beer-Lambert law, which states that the absorbance of a sample is directly proportional to the path length (thickness) and the concentration of the species. A UV lamp generates photons comprising of wavelengths in the ultraviolet and visible, which is transmitted to a beam splitter to generate a reference beam and sample beam. The sample beam passes through the sample of interest and the transmitted intensity is measured relative to the reference beam, from which the absorbance data is obtained. Several parameters like sample thickness, absorption coefficient and also the bandgap of the semiconductor can be derived from the absorbance data.

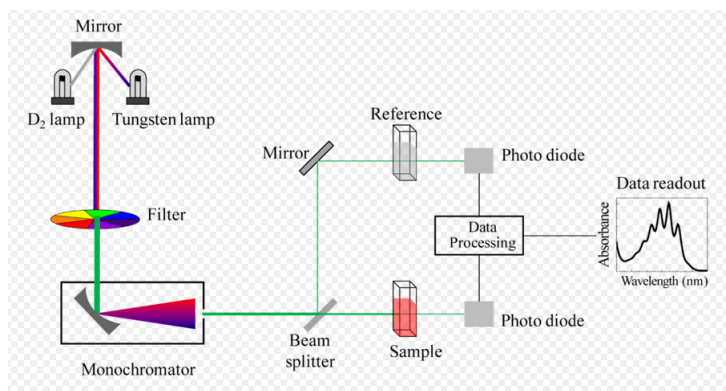


Figure 11 Schematic view of the UV-VIS absorption setup

Absorbance values were obtained from transmittance measurements made by a Cary 5000 UV-VIS spectrophotometer. The absorbance was calculated as

$$A = -\log(T) \quad T - \text{Transmittance}$$

Film thickness was estimated using the Beer Lambert law

$$L = A/\alpha \quad \alpha - \text{absorption coefficient}$$

3.4 CYCLIC VOLTAMMETRY

This technique involves the measurement of the current with application of a voltage that varies linearly with time. Measurements are made in a three electrode cell comprising of a working electrode, counter electrode and a reference electrode, under illumination or in the dark. A potential difference is applied between the working and counter electrodes by means of a potentiostat. The potential of the working electrode is measured with respect to the reference electrode, which in this case is a Ag/AgCl electrode. The counter electrode used is a Platinum wire. Scans were made at a sweep rate of 50 mV/s under 1 sun (100 mW/cm²) Xe-lamp illumination in a Potassium Phosphate buffer (pH 6.55) using a FRA equipped PGSTAT-30 from Autolab and a Keithley 2612 system sourcemeter.

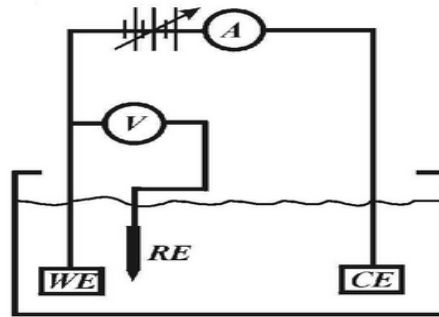


Figure 12 Three electrode setup with working (WE), counter (CE) and reference (RE) electrodes

3.5 ELECTROCHEMICAL IMPEDANCE SPECTROSCOPY (EIS)

In general, impedance spectroscopy involves the application of a frequency-dependent perturbation to a system at steady-state. It consists of the AC measurement of the current, $\tilde{I}(\omega)$ by applying a voltage perturbation $\tilde{V}(\omega)$ or vice versa to obtain the frequency-dependent impedance $Z(\omega)$.

$$Z(\omega) = \tilde{V}(\omega) / \tilde{I}(\omega)$$

It is of crucial importance that the perturbation is small in order to maintain the linear form of the impedance as shown. Ideally, during an impedance measurement, the system is kept at steady-state by imposing stationary conditions such as fixed DC current, illumination intensity etc. The system then obtains the impedance and scans over a range of frequencies, generally ranging a few decades. This procedure is repeated over a range of steady-state voltages to observe the evolution of the parameters with the voltage.

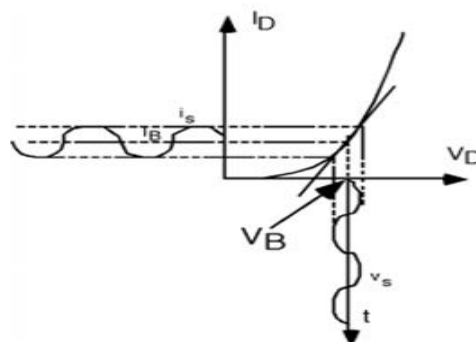


Figure 13 Small signal linear response of the perturbing voltage required for EIS

Using the acquired data, the system is then modelled using the following electrical components:


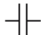

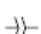
Denomination	Symbol	Scheme	Impedance
Resistance	R		R
Capacitance	C		$\frac{1}{i\omega C}$
Inductor	L		$i\omega L$
Constant phase element (CPE)	Q_n		$\frac{(i\omega)^{-n}}{Q_n}$

Figure 14 Basic electric components used for modelling EIS data and their corresponding impedances

A CPE is used to represent the fact that it is extremely difficult to obtain a purely capacitive response from a system. When the index $n = 1$, we obtain a purely capacitive response but it is often necessary to use $n < 1$ during the fitting of impedance data.

EIS measurements were made in the same 3-electrode configuration as described in section 2.4. The range of potential applied was 0.1 – 1.5 V with a step size of 0.05 V. The applied perturbation amplitude (rms) was 0.02 V and the frequency range of the scan was 0.05 – 100000 hz.

4.1 MICROSCOPY

The morphology of a $\text{SnO}_2/\text{BiVO}_4$ sample was determined by Scanning Electron Microscopy measurements, shown in figure 15. The film appears polycrystalline, with a degree of porosity. Large grain sizes are observed (> 500 nm) with many voids between them, though the film is compact. A clear differentiation between the different phases ($\text{FTO}/\text{SnO}_2/\text{BiVO}_4$) is not observed.

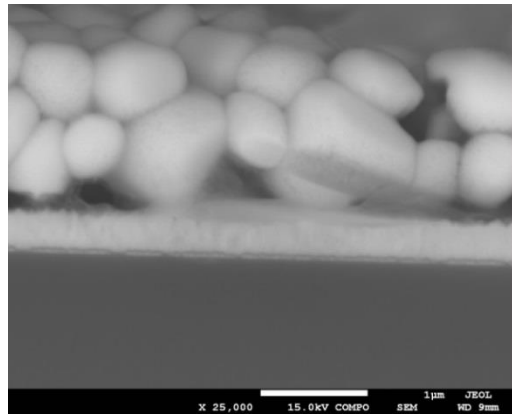


Figure 15 SEM image of $\text{SnO}_2/\text{BiVO}_4$ sample

4.2 X-Ray Diffraction

Crystalline phase of the BiVO_4 samples was determined using X-Ray Diffraction (figure 16), carried out at TUD, Netherlands. Our samples clearly exist in the monoclinic Scheelite phase of BiVO_4 with the data fitted using PDF 14-688 for the planes and their corresponding 2-theta angles.

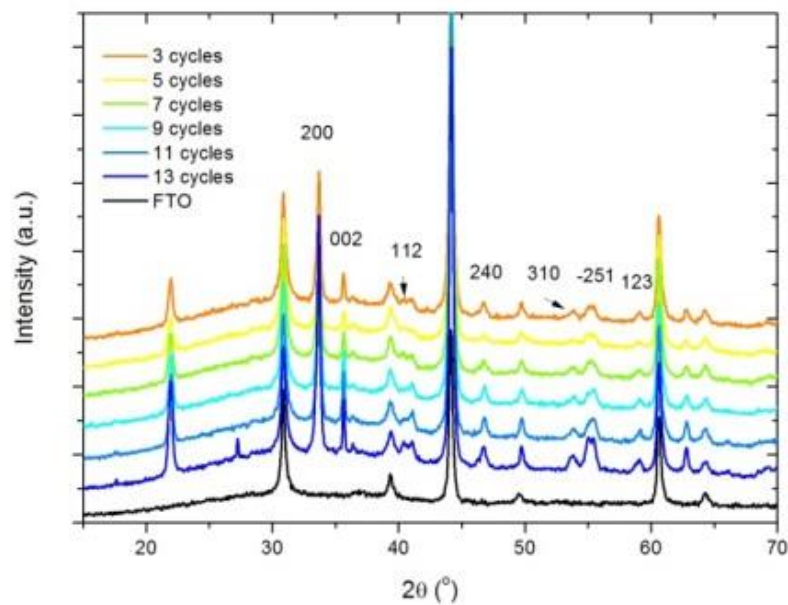


Figure 16 2θ scan results for samples with their respective number of spincoating cycles

4.3 OPTICAL MEASUREMENTS

The optical density of the films was determined from transmittance measurements. Figure 17 shows the absorbance calculated from transmittance measurements and Table 1 provides the estimated values of thickness from these optical measurements, with an absorption coefficient of 30000 for BiVO₄ at 400 nm [15].

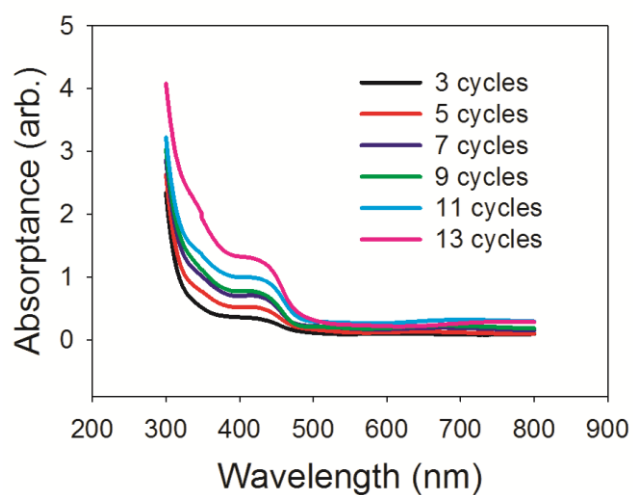


Figure 17 Absorbance of BiVO₄ samples prepared by 3, 5, 7, 9, 11 and 13 cycles of spin-coating

No. of Cycles	Thickness (nm)
3	120
5	174
7	233
9	257
11	332
13	442

Table 1 Calculated thickness (absorption coefficient = $3 \times 10^4 \text{ cm}^{-1}$ at 400 nm) of BiVO₄ samples prepared by 3, 5, 7, 9, 11 and 13 cycles of spin-coating

4.4 Photoelectrochemical (PEC) tests

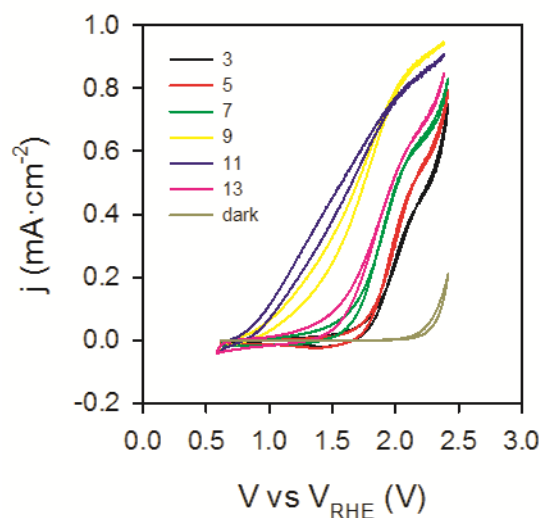


Figure 18 Comparison of substrate (back) illumination of BiVO_4 samples prepared by 3, 5, 7, 9, 11 and 13 cycles of spin-coating as shown in legend

The variation of the PEC performance under illumination with thickness of the BiVO_4 film is shown in figure 18. Two important factors to be noted are the onset potential and the photocurrent at moderately high potentials ($V_{\text{onset}} < V < 1.5 \text{ V}$), as the current at high positive potentials is mainly due to charge transfer of carriers from the valence band. The onset potential is very high for the thinnest sample (3 cycles), $\sim 1.6 \text{ V vs } V_{\text{RHE}}$. With increasing thickness, there is a corresponding cathodic shift in the onset potential, with a value of $\sim 0.6 - 0.8 \text{ V vs } V_{\text{RHE}}$ for the 11 cycles sample. It is also noted that the onset potential is shifted anodically for the thickest sample (13 cycles). The photocurrent also follows a similar trend (figure 19), with a maximum photocurrent density of 0.194 mA/cm^2 at $1.23 \text{ V vs } V_{\text{RHE}}$ for the 11 cycles ($\sim 330 \text{ nm}$ thickness) sample, followed by a reduction in the performance for the thickest sample.

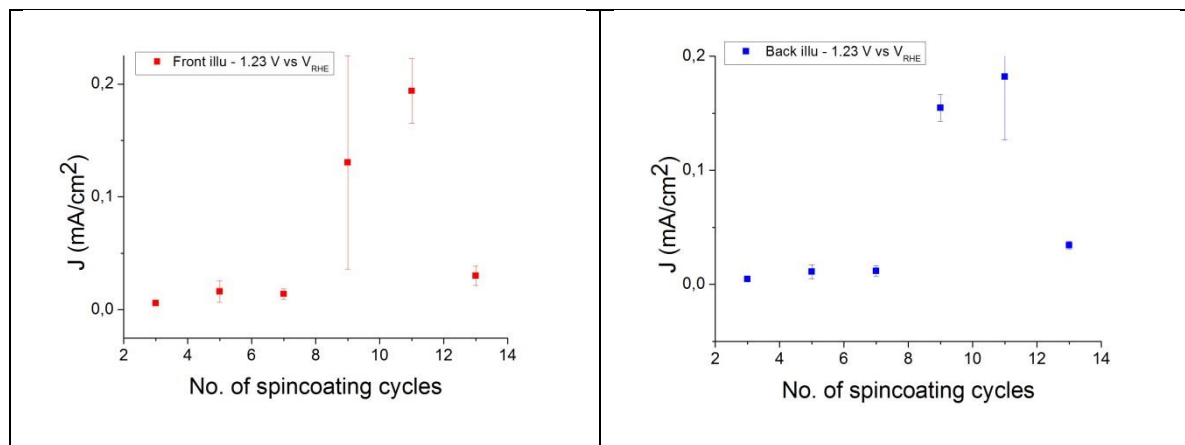


Figure 19 Variation of current density versus thickness of BiVO_4 represented by the number of spincoating cycles (error bars for measurements over 2 samples of each thickness)

An explanation of these trends can be made by considering the diffusion length of the holes, which are the minority carriers, reported to be ~ 100 nm [39]. The PEC performance is determined by the competition between increased absorbance, which generates more electron-hole pairs for extraction, and the thickness of the film over which the carriers have to diffuse to the surface for extraction in relation to the diffusion lengths (The length over which the carrier diffuses before recombination or extraction) of electrons and holes in BiVO_4 . Due to its porous morphology as observed in Figure 15, it is plausible that the diffusion of electrons is the limiting factor for performance. From figure 18, it is clear that the absorption increases with increasing thickness for all the samples, which can explain the increasing photocurrent and corresponding cathodic shift of the onset potential. With the increasing thickness however, the length over which the holes need to diffuse for extraction increases, leading to higher recombination until finally, this limitation counteracts the increased absorption to give an overall reduction in performance, as is observed for the thickest sample (13 cycles). Another factor that could also contribute is the porosity of the samples, which would allow extraction of the holes to the electrolyte without the requirement of diffusion to the top surface, which would explain the improvement of the photocurrent for thicknesses greater than the diffusion length.

A comparison between the performance of front and back illumination is shown in figure 18 and 19. Contrary to the reports described in section 2.3.1, we observe no obvious difference in the performances over the entire range of thicknesses (110 – 450 nm). The slow electron transport described in section 2.3.1 were observed for samples with thickness ~ 200 nm.

In order to identify any limitations in performance due to kinetics at the interface and determine the maximum photocurrent, BiVO_4 with thickness ~ 230 nm (7 cycles spincoating) was tested in a Phosphate buffer (pH 6.55) containing 0.1 M H_2O_2 as hole scavenger. The results are shown in

figure 20.

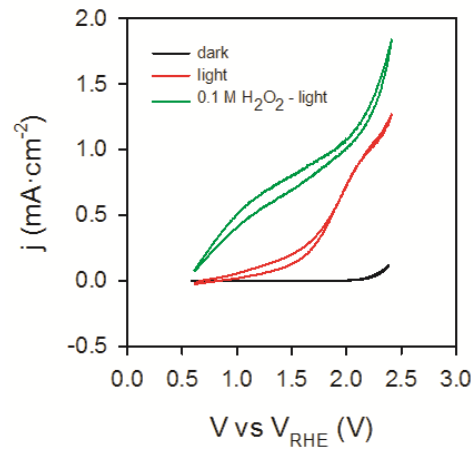


Figure 20 J-V curves in the dark, under illumination and in the presence of a hole scavenger under illumination

We observe a large enhancement ($\sim 0.5 \text{ mA/cm}^2$ at $1.23 \text{ V vs } V_{\text{RHE}}$) in the photocurrent and a cathodic shift in the onset potential upon addition of a hole scavenger. The addition of H_2O_2 improves the kinetics at the $\text{BiVO}_4/\text{electrolyte}$ interface. H_2O_2 has a much higher oxidation rate constant than water due to its more negative reduction potential ($+0.68 \text{ vs } V_{\text{RHE}}$) and the fact that it requires only two holes to be oxidised compared to four for water oxidation [5]. The large improvement in performance confirms the slow water oxidations kinetics at the $\text{BiVO}_4/\text{electrolyte}$ interface, where the slow kinetics of charge transfer leads to a loss of carriers by accumulation and large amount of surface recombination.

4.5 Interfacial SnO_2 layer

To improve the PEC performance, prior to deposition of BiVO_4 (7 cycles spincoating), an interfacial Tin Oxide layer was deposited on the FTO with thickness $\sim 100 \text{ nm}$ at TU-DELFT by automatic spray pyrolysis. The performances of the $\text{FTO}/\text{SnO}_2/\text{BiVO}_4$ samples are shown in

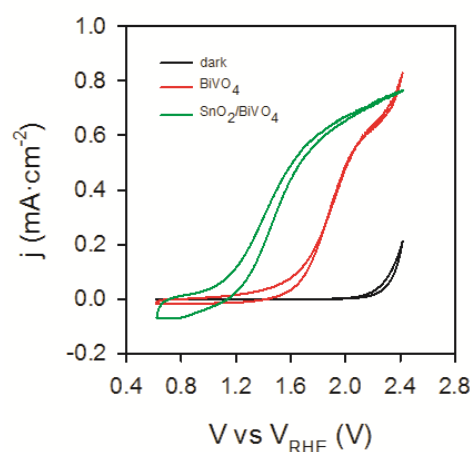


Figure 21 Comparison in performance of BiVO_4 (7 cycles spincoating) with and without an interfacial Tin Oxide layer

figure 21.

A large enhancement in photocurrent (~ 0.55 mA at 1.6 V vs V_{RHE}) in the moderate to high potential range along with a cathodic shift in the onset potential of a few 100 mV is observed. These results confirm the beneficial effect of the interfacial SnO_2 layer, as described in reports.

5.6 EIS MEASUREMENTS

In this section, we investigate the carrier dynamics of the BiVO_4 system by impedance spectroscopy in order to identify the various charge-transfer processes, resistances and capacitances contributing to the water oxidation process. Important information regarding the space-charge capacitance at the interface including the flatband potential and doping densities will give an idea about the performance and limitations of this photoanode.

EIS measurements were carried out on the samples in the dark and the obtained results, including the fitting circuit, is shown in figure 22 and 23.

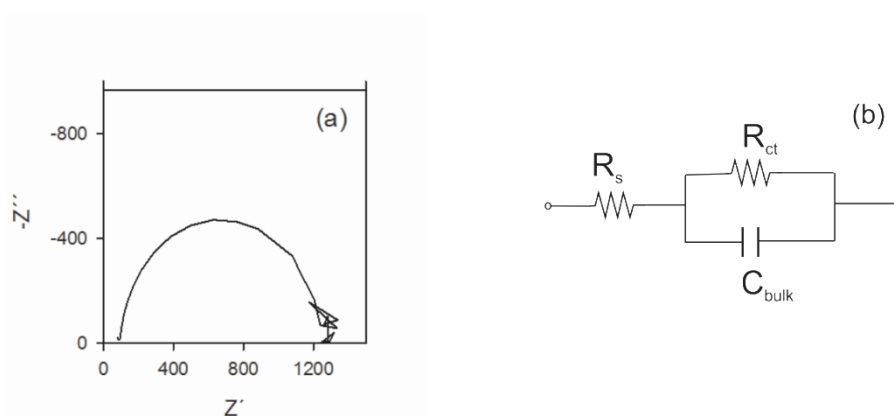


Figure 22 a) Nyquist plot of 7 cycles spincoating BiVO_4 sample at 1.4 V vs $V_{\text{Ag/AgCl}}$ b) Fitting circuit used for the EIS data in dark

The observed single arc in the Nyquist plot is typical of a resistor and capacitor in parallel, with a resistor in series displacing the arc along the real axis, which was the fitting circuit used. A CPE was used instead of a capacitor, from which the capacitance values (figure 23) were extracted using the Brug formula [40].

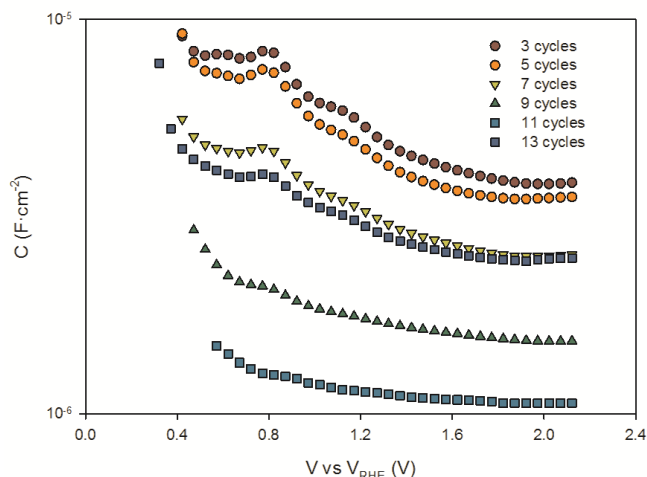


Figure 23 Variation of capacitance with applied voltage of BiVO_4 samples of different thicknesses obtained from EIS measurements in dark conditions

The obtained capacitance values are of the order of 10^{-6} F, which are similar values to that obtained for Haematite photoanodes for a space-charge/bulk capacitance [41, 42]. Similar values have also been reported for BiVO_4 photoanodes [13,22,40,41]. Fitting of surface states model developed by Bisquert [43] yielded no evidence of the existence of surface states in the dark (fitting not included), which points favorably to the fact that the observed capacitance is indeed the space charge capacitance at the surface.

With the assumption that the observed capacitance is the space charge capacitance at the surface (band bending), Mott-Schottky plots were generated (figure 24) and obtained flatband potentials with corresponding literature values are shown in table 2. Large positive values for the flatband potentials for 3, 5, 7 and 9 cycles of spincoating are observed. There also exists a peak in the capacitance at ~ 0.75 V vs V_{RHE} , which is the potential of the $\text{V}^{4+}/\text{V}^{5+}$ redox couple [44]. The fitting of the straight line to obtain the flatband potential has been carried out between 0.8 -1.8 V vs V_{RHE} , without including the capacitance peak, which could alter the actual flatband value.

Number of spincoating cycles	V_{fb} vs V_{RHE} (V)	Donor density $\cdot 10^{18}$ (cm^{-3})	Reference	V_{fb} vs V_{RHE} (V)
3	+0.6	42.6	Seabold et al [13]	≈ -0.07
5	+0.52	33	Sayama et al [45]	$\approx +0.02$
7	+0.5	13.3	Berglund et al [22]	≈ -0.08
9	-0.21	7.7	Rettie et al [46]	$\approx +0.03 - 0.08$
11	-0.05	4.5		
13	+0.25	26.6		

Table 2 Obtained Flatband Potentials and Doping density values from EIS measurements, flatband potentials obtained from literature

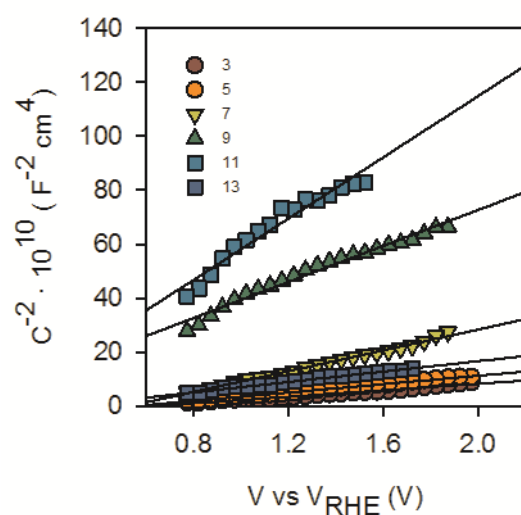


Figure 24 Mott-Schottky plots of BiVO_4 samples of different thicknesses represented by number of spincoating cycles shown in legend obtained from EIS measurements in dark conditions

The large deviation of the obtained flatband values, especially for samples of 3, 5, 7 and 9 cycles of spincoating, are an indicator that either the attribution of the observed capacitance to a space-charge capacitance is erroneous or the fact that the space-charge capacitance is coupled with another capacitance.

The variations in flatband potentials could be related to the changes in doping densities, which is a bulk property. This points to the fact that there are variations in composition of the samples, possibly due to naturally occurring defects and other variations during synthesis. Variations in the Helmholtz potential at the interface can be caused by the charging of surface states, which alters the flatband value by band unpinning [47]. Another factor is the variation in surface roughness for the different samples, which can alter the capacitance at the interface and hence cause a variation in the flatband potential value. Since we do not have any evidence of the existence of surface states in dark from the EIS measurements, a further investigation must be made in the future to determine the variations in surface roughness and the bulk composition of the samples to understand the variations in flatband potentials and doping densities with thickness.

Another interesting observation is the comparison between flatband potentials and onset potentials. The obtained onset potentials for 7 cycles spincoated BiVO₄ samples in the presence of a hole scavenger (figure 20) are very similar to the obtained flatband potentials (Table 2), while the onset potential is more positive for BiVO₄ samples in the absence of a hole scavenger. This shows that while a large potential difference exists for driving the holes from the valence band of BiVO₄, the major limitation in performance is the kinetics at the interface.

In conclusion, the thickness dependent study on bismuth vanadate photoanodes has shown that:

- Bismuth Vanadate is a promising photoanode, with maximum obtained performance of 0.194 mA/cm^2 at $1.23 \text{ V vs } V_{\text{RHE}}$ for a bare BiVO_4 sample with thickness $\sim 330 \text{ nm}$
- PEC performance scales with thickness until a limiting value ($\sim 330 \text{ nm}$), related to the trade-off between increased absorption and lengths of diffusion for the carriers
- Water oxidation kinetics at the $\text{BiVO}_4/\text{H}_2\text{O}$ interface is very slow, leading to high surface recombination
- There exists no discernible difference in performance of front and back illumination over a range of thickness of the samples, lack of evidence of slow electron transport
- An interfacial SnO_2 layer deposited on the FTO prior to BiVO_4 deposition enhances the PEC performance in the moderate to high potential range with a cathodic shift in onset potential
- Further investigations are required for:
 - Confirmation of the observed capacitance in EIS measurements as indeed the space-charge capacitance
 - Investigation of surface roughness of the samples to identify effect on Helmholtz layer and hence flatband potential
 - Investigation of the degree of porosity of the spincoated samples
 - Clarification of the mechanism of SnO_2 interfacial layer PEC performance enhancement
 - Understanding the claim of slow electron transport in BiVO_4
 - Optimisation of thickness of SnO_2 layer to maximise PEC performance

BIBLIOGRAPHY

1. Lewis, N.S. and G. Crabtree, *Basic research needs for solar energy utilization: report of the basic energy sciences workshop on solar energy utilization, April 18-21, 2005*. 2005.
2. Walter, M.G., et al., *Solar Water Splitting Cells*. Chemical Reviews, 2010. **110**(11): p. 6446-6473.
3. Hong, S.J., et al., *Heterojunction BiVO₄/WO₃ electrodes for enhanced photoactivity of water oxidation*. Energy & Environmental Science, 2011. **4**(5): p. 1781-1787.
4. Zhong, D.K., S. Choi, and D.R. Gamelin, *Near-Complete Suppression of Surface Recombination in Solar Photoelectrolysis by "Co-Pi" Catalyst-Modified W:BiVO₄*. Journal of the American Chemical Society, 2011. **133**(45): p. 18370-18377.
5. Abdi, F.F. and R. van de Krol, *Nature and Light Dependence of Bulk Recombination in Co-Pi-Catalyzed BiVO₄ Photoanodes*. The Journal of Physical Chemistry C, 2012. **116**(17): p. 9398-9404.
6. Berglund, S.P., et al., *Incorporation of Mo and W into nanostructured BiVO₄ films for efficient photoelectrochemical water oxidation*. Physical Chemistry Chemical Physics, 2012. **14**(19): p. 7065-7075.
7. Sleight, A.W., et al., *Crystal growth and structure of BiVO₄*. Materials Research Bulletin, 1979. **14**(12): p. 1571-1581.
8. Dreyer, G. and E. Tillmanns, *Dreyerite-Natural, Tetragonal Bismuth Vanadate from Hirschhorn-Pfalz*. Neues Jahrbuch fur Mineralogie-Monatshefte, 1981(4): p. 151-154.
9. Park, Y., K.J. McDonald, and K.-S. Choi, *Progress in bismuth vanadate photoanodes for use in solar water oxidation*. Chemical Society Reviews, 2013. **42**(6): p. 2321-2337.
10. Kudo, A., K. Omori, and H. Kato, *A Novel Aqueous Process for Preparation of Crystal Form-Controlled and Highly Crystalline BiVO₄ Powder from Layered Vanadates at Room Temperature and Its Photocatalytic and Photophysical Properties*. Journal of the American Chemical Society, 1999. **121**(49): p. 11459-11467.
11. Liang, Y., et al., *Highly Improved Quantum Efficiencies for Thin Film BiVO₄ Photoanodes*. The Journal of Physical Chemistry C, 2011. **115**(35): p. 17594-17598.
12. Trzesniewski, B.J. and W.A. Smith, *Photocharged BiVO₄ photoanodes for improved solar water splitting*. Journal of Materials Chemistry A, 2015.
13. Seabold, J.A. and K.-S. Choi, *Efficient and Stable Photo-Oxidation of Water by a Bismuth Vanadate Photoanode Coupled with an Iron Oxyhydroxide Oxygen Evolution Catalyst*. Journal of the American Chemical Society, 2012. **134**(4): p. 2186-2192.
14. Dall'Antonia, L.H., et al., *Electrosynthesis of Bismuth Vanadate Photoelectrodes*. Electrochemical and Solid-State Letters, 2010. **13**(5): p. D29-D32.

15. Chen, Y.-S., J.S. Manser, and P.V. Kamat, *All Solution-Processed Lead Halide Perovskite-BiVO₄ Tandem Assembly for Photolytic Solar Fuels Production*. Journal of the American Chemical Society, 2015. **137**(2): p. 974-981.
16. Su, J., et al., *Nanostructured WO₃/BiVO₄ Heterojunction Films for Efficient Photoelectrochemical Water Splitting*. Nano Letters, 2011. **11**(5): p. 1928-1933.
17. Bhattacharya, A.K., K.K. Mallick, and A. Hartridge, *Phase transition in BiVO₄*. Materials Letters, 1997. **30**(1): p. 7-13.
18. Yao, W. and J. Ye, *Photophysical and Photocatalytic Properties of Ca_{1-x}BixV_xMo_{1-x}O₄ Solid Solutions*. The Journal of Physical Chemistry B, 2006. **110**(23): p. 11188-11195.
19. Walsh, A., et al., *Band Edge Electronic Structure of BiVO₄: Elucidating the Role of the Bi s and V d Orbitals*. Chemistry of Materials, 2009. **21**(3): p. 547-551.
20. Chatchai, P., et al., *Efficient photocatalytic activity of water oxidation over WO₃/BiVO₄ composite under visible light irradiation*. Electrochimica Acta, 2009. **54**(3): p. 1147-1152.
21. Saito, R., Y. Miseki, and K. Sayama, *Highly efficient photoelectrochemical water splitting using a thin film photoanode of BiVO₄/SnO₂/WO₃ multi-composite in a carbonate electrolyte*. Chemical Communications, 2012. **48**(32): p. 3833-3835.
22. Berglund, S.P., et al., *Photoelectrochemical Oxidation of Water Using Nanostructured BiVO₄ Films*. The Journal of Physical Chemistry C, 2011. **115**(9): p. 3794-3802.
23. Luo, W., et al., *Solar hydrogen generation from seawater with a modified BiVO₄ photoanode*. Energy & Environmental Science, 2011. **4**(10): p. 4046-4051.
24. Kim, T.W. and K.-S. Choi, *Nanoporous BiVO₄ Photoanodes with Dual-Layer Oxygen Evolution Catalysts for Solar Water Splitting*. Science, 2014. **343**(6174): p. 990-994.
25. Su, J., et al., *Aqueous Growth of Pyramidal-Shaped BiVO₄ Nanowire Arrays and Structural Characterization: Application to Photoelectrochemical Water Splitting*. Crystal Growth & Design, 2010. **10**(2): p. 856-861.
26. Morris Hotsenpiller, P.A., et al., *Orientation Dependence of Photochemical Reactions on TiO₂ Surfaces*. The Journal of Physical Chemistry B, 1998. **102**(17): p. 3216-3226.
27. Hugen Schmidt, M.B., L. Gamble, and C.T. Campbell, *The interaction of H₂O with a TiO₂(110) surface*. Surface Science, 1994. **302**(3): p. 329-340.
28. Choi, K.-S., *Shape Effect and Shape Control of Polycrystalline Semiconductor Electrodes for Use in Photoelectrochemical Cells*. The Journal of Physical Chemistry Letters, 2010. **1**(15): p. 2244-2250.
29. Yang, H.G., et al., *Anatase TiO₂ single crystals with a large percentage of reactive facets*. Nature, 2008. **453**(7195): p. 638-641.
30. Zhou, M., et al., *C-oriented and {010} Facets Exposed BiVO₄ Nanowall Films: Template-Free Fabrication and their Enhanced Photoelectrochemical Properties*. Chemistry – An Asian Journal, 2010. **5**(12): p. 2515-2523.
31. Fan, H., et al., *Effect of BiVO₄ Crystalline Phases on the Photoinduced Carriers Behavior and Photocatalytic Activity*. The Journal of Physical Chemistry C, 2012. **116**(3): p. 2425-2430.
32. Wang, D., et al., *Crystal Facet Dependence of Water Oxidation on BiVO₄ Sheets under Visible Light Irradiation*. Chemistry – A European Journal, 2011. **17**(4): p. 1275-1282.
33. Xi, G. and J. Ye, *Synthesis of bismuth vanadate nanoplates with exposed {001} facets and enhanced visible-light photocatalytic properties*. Chemical Communications, 2010. **46**(11): p. 1893-1895.
34. Park, H.S., et al., *Factors in the Metal Doping of BiVO₄ for Improved Photoelectrocatalytic Activity as Studied by Scanning Electrochemical Microscopy and*

- First-Principles Density-Functional Calculation*. The Journal of Physical Chemistry C, 2011. **115**(36): p. 17870-17879.
35. Zhao, Z., Z. Li, and Z. Zou, *Electronic structure and optical properties of monoclinic clinobisvanite BiVO₄*. Physical Chemistry Chemical Physics, 2011. **13**(10): p. 4746-4753.
 36. Pilli, S.K., et al., *Cobalt-phosphate (Co-Pi) catalyst modified Mo-doped BiVO₄ photoelectrodes for solar water oxidation*. Energy & Environmental Science, 2011. **4**(12): p. 5028-5034.
 37. Wang, D., et al., *Photocatalytic Water Oxidation on BiVO₄ with the Electrocatalyst as an Oxidation Cocatalyst: Essential Relations between Electrocatalyst and Photocatalyst*. The Journal of Physical Chemistry C, 2012. **116**(8): p. 5082-5089.
 38. Jeon, T.H., W. Choi, and H. Park, *Cobalt-phosphate complexes catalyze the photoelectrochemical water oxidation of BiVO₄ electrodes*. Physical Chemistry Chemical Physics, 2011. **13**(48): p. 21392-21401.
 39. Chen, L., et al., *Reactive Sputtering of Bismuth Vanadate Photoanodes for Solar Water Splitting*. The Journal of Physical Chemistry C, 2013. **117**(42): p. 21635-21642.
 40. Brug, G.J., et al., *The analysis of electrode impedances complicated by the presence of a constant phase element*. Journal of Electroanalytical Chemistry, 1984. **176**(1-2): p. 275-295.
 41. Klahr, B., et al., *Photoelectrochemical and impedance spectroscopic investigation of water oxidation with "Co-Pi"-coated hematite electrodes*. Journal of the American Chemical Society, 2012. **134**(40): p. 16693-16700.
 42. Klahr, B., et al., *Water Oxidation at Hematite Photoelectrodes: The Role of Surface States*. Journal of the American Chemical Society, 2012. **134**(9): p. 4294-4302.
 43. Bisquert, J., *Theory of the impedance of charge transfer via surface states in dye-sensitized solar cells*. Journal of Electroanalytical Chemistry, 2010. **646**(1-2): p. 43-51.
 44. Qin, D.-D., et al., *Reduced monoclinic BiVO₄ for improved photoelectrochemical oxidation of water under visible light*. Dalton Transactions, 2014. **43**(21): p. 7691-7694.
 45. Sayama, K., et al., *Photoelectrochemical Decomposition of Water into H₂ and O₂ on Porous BiVO₄ Thin-Film Electrodes under Visible Light and Significant Effect of Ag Ion Treatment*. The Journal of Physical Chemistry B, 2006. **110**(23): p. 11352-11360.
 46. Rettie, A.J.E., et al., *Combined Charge Carrier Transport and Photoelectrochemical Characterization of BiVO₄ Single Crystals: Intrinsic Behavior of a Complex Metal Oxide*. Journal of the American Chemical Society, 2013. **135**(30): p. 11389-11396.
 47. Kelly, J.J. and R. Memming, *The Influence of Surface Recombination and Trapping on the Cathodic Photocurrent at p-Type III-V Electrodes*. Journal of The Electrochemical Society, 1982. **129**(4): p. 730-738.